MORPHOLOGY AND MECHANICS OF CORTICAL FOLDING ASSOCIATED WITH AUDITORY DEPRIVATION

by

Qianwei Li

A thesis submitted to Johns Hopkins University

in conformity with the requirements for the degree of

Master of Science in Engineering

Baltimore, Maryland

May, 2021

Abstract

Hearing loss is increasingly becoming a common disabling condition that affects the global population. Functional and structural changes occur in the developing auditory cortex after the onset of auditory deprivation. This study aims at measuring and modeling these changes, which can help understand the pathology of hearing loss and support research on treatment. Specifically, it describes a pipeline of automatically extracting inner and outer cortical surfaces from MRI images and measuring morphological metrics. Then, a two-component finite element mechanical model mimicking gray matter and white matter is used to investigate the causes of measured structural differences between cats with normal hearing and hearing loss. Mechanical parameters, such as shear and bulk modulus, are varied with a view to studying their influence on cortical folding patterns. Compared to hearing cats, cats with hearing loss have decreased cortical curvature and folding index, and increased thickness. By varying the shear modulus and bulk modulus of the gray and white matter at different locations, the mechanical model reveals distinct stable folding patterns. Specific combinations of parameters and locations lead to changes in curvature, folding index, and thickness. The methods used in this study can also be extended to examine cortical morphological characteristics

associated with other abnormalities in the developing brain.

Thesis Readers

Dr. Tilak Ratnanather (Primary Advisor)

    Associate Research Professor

    Department of Biomedical Engineering

    Johns Hopkins University

Dr. Kwame Kutten

    Lecturer

    Department of Biomedical Engineering

    Johns Hopkins University

Dr. Vikram Chib

    Assistant Professor

    Department of Biomedical Engineering

    Johns Hopkins University

Acknowledgments

I would like to thank my advisior Dr. Tilak Ratnanather, Dr. Kwame Kutten and Dr. Peter Hubka for their invaluable guidance and feedback throughout my work. I would also like to thank Dr. Vikram Chib for reviewing my thesis.

I would like to extend my gratitude to all my teachers and friends for spending an unforgettable time with me.

I am forever grateful to my mother and father for their unwavering love, support, and encouragement throughout my life. All my accomplishments would not have been possible without them.

Table of Contents

List of Tables

List of Figures

Chapter 1

Introduction

1.1   Hearing Loss and Brain Development

Hearing loss is indicated by decreased auditory sensitivity, increased hearing threshold, auditory system dysfunction, and deafness. Abnormalities of the auditory system, including the hair cells, the auditory nerve, or the auditory cortex, will reduce auditory function, causing difficulty with communication. There are multiple causes of hearing loss, such as genetic factors, aging, noise, and ototoxicity. According to World Health Organization (WHO) survey, 5 % of the world's population have disabling hearing disorder (WHO, 2021), so WHO estimates that nearly 450 million people will have diasbling hearing loss by 2050, so hearing loss is increasingly becoming a common condition that affects the development as well as the quality of life.

Congenital hearing loss is often caused by abnormalities of the outer, middle, and inner ear, including structural malformations, cochlear hair cell damage, and auditory neuropathy (Korver et al., 2017). However, not limited to these areas, hearing loss also affects the central auditory system. Since the

brain has neuroplasticity, the normal establishment of auditory function in development depends on sound stimulation in the early postnatal period. The ability to receive auditory signal input is significantly reduced or even lost in children with hearing loss. Therefore, the development of the auditory cortex, auditory-sensory cortex, and visual-sensory cortex is affected, which eventually leads to structural and functional changes and reorganization of several related brain areas (Manno et al., 2021; Ratnanather, 2020). Consequently, people with hearing loss not only have abnormal auditory cortex functions, but also have difficulties in speech perception and comprehension.

Studies on cochlear abnormalities have shown that although earlier intervention results in more activation of the auditory cortex, reduced function persists even after cochlear implantation (Feng et al., 2018; Kral et al., 2002; Kral et al., 2006). The reason may be irreversible neurological plasticity in brain development, since auditory neurons play a crucial role in the functional and physical structure of brain. Therefore, hearing loss is more than an auditory problem. It can lead to neurological disorder that affects several neural networks jointly participating in brain function remodeling. A key question is, what functional and structural changes occur in the auditory cortex after the onset of hearing loss or after treatment.

Many studies of the functional and structural changes in the central auditory system due to hearing loss stem from animal model experiments. White cats are a common model animal for studying hearing loss (Ryugo & Menotti-Raymond, 2012; Ryugo et al., 1997). Studies have found that inherited congenital deafness in cats occurs almost exclusively in blue-eyed white cats due

to their genetics (Bergsma & Brown, 1971; Heid et al., 1998). Their deafness is correlated with structural abnormalities in the inner ear and may produce unilateral or bilateral deafness (Ryugo & Menotti-Raymond, 2012). In Heid et al. (1998), 72% of the sample was completely deaf. The organ of Corti degenerated during the first few weeks of life. Auditory stimuli did not elicit brainstem responses during these weeks, suggesting that these cats did not experience any auditory sensation. A few months later, their spiral ganglia also begin to degenerate. However, even in adult cats, auditory afferent nerves remain functional. Leake et al. (1999) observed an increased survival rate of spiral ganglion neurons with cochlear implant for long-term electrical stimulation. Kral et al. (2000) found a functional defect in the primary auditory cortex of congenitally deaf cats by comparing synaptic activity in different cortices. These results imply that the auditory nerve is initially well preserved in congenitally deaf cats, and that lack of auditory stimulation can affect afferent nerve and central nervous system development.

1.2   Morphological Metrics and Models

There are multiple anatomical differences in animals with hearing loss compared to animals with normal hearing, such as reductions in the volume of the cochlear nucleus and the size of the primary auditory cortex (Butler & Lomber, 2013). The differences seem to be related to the onset age of hearing loss. However, in addition to volume, other complex morphological features of the auditory cortex and its developmental process are not well understood.

A crucial part of brain development and morphogenesis is cerebral cortex

folding. Most mammals have a highly-folded cortex, whereas the brains of small animals, such as mice, are smooth (Garcia et al., 2018). Research suggests that cortical folding is associated with higher cognitive performance, possibly because this maximizes the use of the brain's computational units and reduces communication costs (Gautam et al., 2015). This thesis provides evidence that cortical folding is associated with function, so it can be a valuable metric for studying brain structure and cognition functions. Metrics of cortical folding, such as curvature, folding index and thickness, may reflect the impact of hearing loss on auditory cortex development. Advanced imaging techniques and mathematical methods are essential to measure these metrics and thus describe the complexity of the auditory cortical structure quantitatively and objectively.

Recently, advances in brain imaging technology have provided powerful tools to explore the cortical changes caused by hearing loss (Ratnanather, 2020). It can help understand the mechanisms of hearing loss development more comprehensively, thus providing a theoretical basis for rehabilitation treatment. Commonly used brain imaging techniques include high-resolution optical imaging, magnetic resonance imaging (MRI), diffusion tensor imaging (DTI), positron emission computed tomography (PET) and x-ray computed tomography (CT). Optical imaging can achieve the highest spatial resolution, but is usually invasive or in vitro. Among the non-invasive techniques, MRI has an excellent spatial resolution, so it is suitable for morphological studies. Since 1980, MRI has been frequently used to obtain anatomical images of small animals (Hansen et al., 1980). MRI-based studies can provide an accurate and

reproducible assessment of structural changes in hearing loss (Nichols et al., 2017; Ratnanather, 2020; Tarabichi et al., 2018). In a meta-analysis of MRI studies, in subjects with congenital hearing loss, grey matter in and white matter underlying the frontal lobe decreased most, with the right hemisphere being more affected than the left (Manno et al., 2021).

Due to the curved shape of the cortex, grey matter thickness can not be measured accuratly along a straight line in an Euclidean coordinate system (Bok, 1959). Thus many methods for approximating cortical thickness in the curved cortex have been proposed, such as Laplacian and registration-based cortical coordinate systems (Das et al., 2009; Jones et al., 2000; Leprince et al., 2015; Ratnanather et al., 2020; Waehnert et al., 2014). Columnar-like coordinate system based on diffeomorphism can generate more realistic 3D coordinates and provide more reliable metrics measurements (Ratnanather et al., 2020). These complex coordinate systems often need a substantial amount of computational resources.

Furthermore, image-based analysis can show structural differences between cats with normal hearing and hearing loss, so here comes the question: how these differences are formed. Continuum mechanics models can simulate tissue behavior in 2D or 3D to study the cortical folding process. Experiments based on mechanical models show that the inhomogeneity of cortex geometry, mechanical properties of the gray and white matter, thickness, or growth can all affect the folding pattern of the cortex (Budday et al., 2015; Budday & Steinmann, 2018; da Costa Campos et al., 2021; Garcia et al., 2018; Toro & Burnod, 2005).

Chapter 2

Surface Reconstruction and Measurements of Structural Metrics

This chapter describes a pipeline of MRI-based metric calculations of auditory cortical structures in cats. The experimental subjects were seven cats: three hearing cats, three bilaterally deaf cats, and one left-sided deaf cat, as shown in Table 2.1.

Cat	Hearing Loss
WK7E3E	No
WK1A66	No
WK7288	No
WK7398	Bilateral
WK00CE	Bilateral
WK7290	Bilateral
WK7281	Left

Table 2.1: Subjects' hearing condition.

As shown in figure 2.1, the first step is to segment the cortex in the MRI image. The second step is to extract a 3D triangular mesh surface model from the segmentation. Next, divide the inner and outer surfaces of the cortex
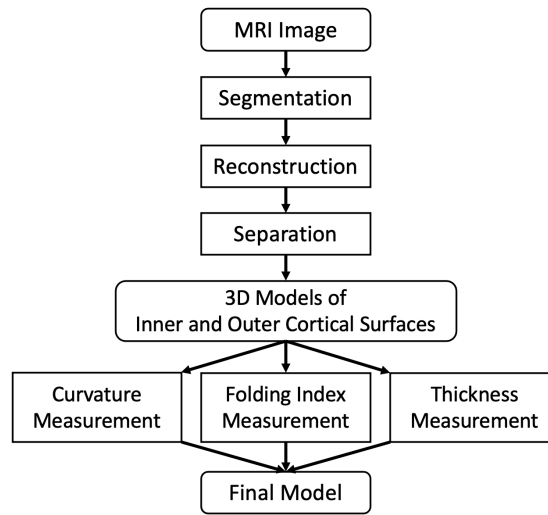
Figure 2.1: A pipeline of measuring structural metrics based on cat MRI images. Rounded rectangles represent data. Rectangles represent operations.

into two models. Calculate the curvature of each vertex using a weighted sum approximation. Create an outer hull surface of the cortex and calculate the folding index (FI) based on corresponding surface points. Register the inner surface to the outer surface, then the cortical thickness is given by the deformation field.

2.1 Segmentation, Surface Reconstruction and Separation

Seed-based binary segmentation of MRI images was performed using 3D Slicer (Fedorov et al., 2012) to extract the cortical segmentation of the ROI region. Due to the limited resolution of MRI, narrow brain sulci boundaries could be mislabeled. Moreover, some errors cause the outer and inner cortical surfaces to be connected at specific locations, usually at the bottom of a sulcus, affecting

the automatic surface separation and measurement. Therefore, manual edits are involved in order to improve the segmentation for easier and more accurate measurement.

After obtaining the segmentation, there are two methods to generate a 3D triangular mesh model of the cortical surfaces, the Marching Cubes and Delaunay Triangulation methods (Chew, 1989; Lorensen & Cline, 1987). Marching Cubes is one of the first and most popular methods, having high speed and simplicity. It creates a triangular mesh by finding those intersect with isosurface in cubes composed of 8 vertexes, and interpolating on cubes' surfaces. However, a cube may have multiple different but all correct triangle divisions, so there are continuity and topological problems between the output mesh and the isosurface. Delaunay Triangulation method can generate more uniform triangular meshes by imposing restrictions on the shape of the triangles. The 3D surface model generated by the latter method is significantly smoother, but it consumes more time and memory. By decimating and smoothing the model generated by the Marching Cubes method, a smoother model can also be obtained. There are subtle shape differences between the two models, especially at locations of large curvature, but the measurements only have limited voxel-level differences. Therefore, in future, when more cat brain images are processed, different methods can be chosen depending on the computational resources.

In order to calculate cortical thickness, it is necessary to divide the inner and outer surfaces of the cortex. There are semi-automatic and automatic methods (Ratnanather et al., 2003). The semi-automatic method is to manually

8

select the vertices at the boundary in Paraview software, connect them into a dividing line, and automatically separate the surfaces on both sides of the dividing line. The automatic method is to find the boundary vertices of the inner and outer surfaces in each frame of the segmentation image, generate the dividing line automatically based on vertices' coordinates in 3D space, and then separate the surfaces using the dividing line. The specific steps are as follows.

Step 1: Apply erode, dilate and median blur filters to the original image, in order to simplify the skeleton and make the boundary smoother.

Step 2: Perform skeletonization using FilFinder (Koch & Rosolowsky, 2015),
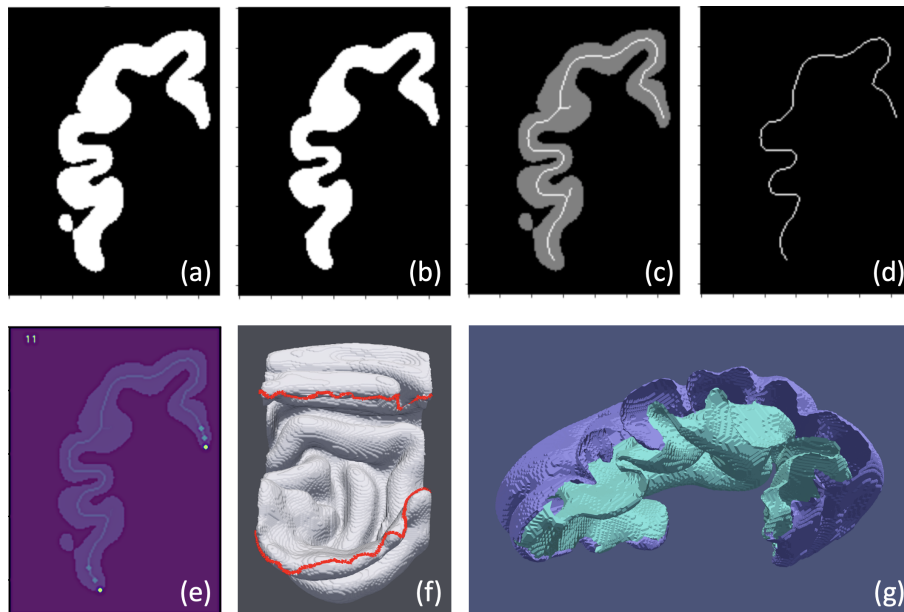
Figure 2.2: Visualization of steps of dividing the inner and outer surfaces of the cortex. (a) A frame of the original segmentation. (b) Result of applying erode, dilate, and median blur filters. (c) Skeleton of image. (d) The primary path of the skeleton. (e) The extended path(green) and its intersection(yellow) with the contour. (f) Dividing line (red) on the surface model. (g) Divided inner (green) and outer (purple) cortical surfaces.

9

and select the longest one as the primary path.

Step 3: Generate the contour of binary segmentation using OpenCV (Bradski, 2000).

Step 4: Extend the main path outward in the direction of the end, and find the intersection points with the contour. These two intersection points are the dividing points between the inner and outer surfaces. Record the 2D coordinates of the dividing points plus the frame index as 3D coordinates.

Step 5: For each frame, perform steps 1-4 to obtain the coordinates of the dividing points. Convert their coordinates to the 3D model space. Find the closest vertex to each point among the vertices of the 3D model. They are the dividing vertices of the outer and inner cortical surfaces.

Step 6: Find the shortest paths between adjacent dividing vertices using curvature based dynamic programming (Dijkstra et al., 1959; Ratnanather et al., 2003). Combine all paths to form the dividing line.

Step 7: Remove the vertices through which the dividing line passes. Find the connected components of the 3D model. Theoretically, there should be two connected components, i.e., inner and outer surfaces. However, inaccurate segmentation may generate isolated fragmented pieces, resulting in more than two connected components. These pieces are usually tiny and do not affect the final results. Therefore, select the

two connected components with the maximum number of cells as the inner and outer surfaces.

2.2 Curvature

Curvature describes the degree to which a curve deviates from a straight line or a surface deviates from a plane. The number of curves past a point on a surface is infinite, so is the number of curvatures. These curvatures are called normal curvatures. The normal curvature with the maximum value is k_1. k_2 is the curvature perpendicular to the normal plane associated with k_1. k_1 and k_2 are the principal curvatures, having maximum and minimum value. The tangent directions of the corresponding curves are called the principal curvature directions, which are the steepest and smoothest directions.

Although the two principal curvatures are more informative, one would
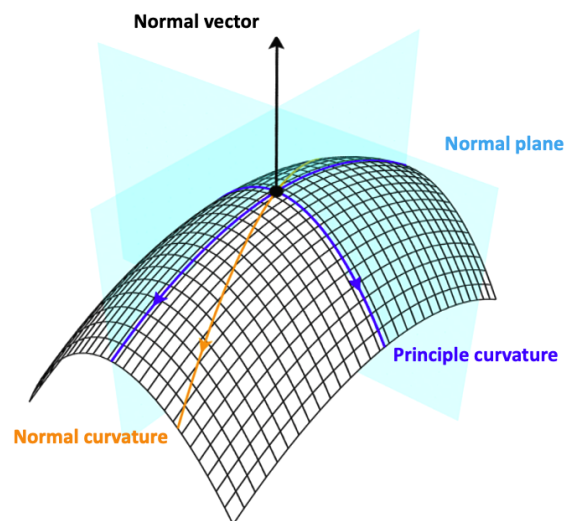
Figure 2.3: An example of surface curvature.
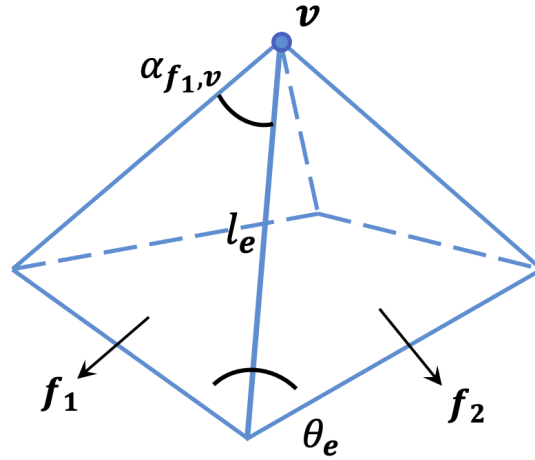
Figure 2.4: An example of triangular mesh model. v is a vertex. f_1 and f_2 are two neighbor faces of v, intersecting at edge e. $\alpha_{f_1,v}$ is the angle of f_1 at v. l_e is the length of e. θ_e is the exterior dihedral angle between f_1 and f_2

prefer a single shape indicator rather than a pair of numbers, such as the mean curvature and the Gaussian curvature.

The mean curvature, $H = (k_1 + k_2)/2$, is the average of the principal curvatures, equal to the average of all normal curvatures. It measures the degree of curving of a surface embedded in space.

The Gaussian curvature, $K = k_1 * k_2$, is equal to the product of principal curvatures. It measures the intrinsic curvature of a surface, which remains constant under isometric transformations of the surface. Any non-stretching transformation of a surface will not change its Gaussian curvature. For example, a plane has a Gaussian curvature of 0. If it is bent into the side of a cylinder, its Gaussian curvature is still 0. Therefore, it can represent the intrinsic characteristics of the surface.

Our triangular mesh model is a discrete surface consisting of vertices and triangle faces, as shown in Figure 2.4. Its curvature is estimated using a

weighted sum. The formulas are as follows.

$$
\begin{aligned}
\text{Mean Curvature :} \quad & H(v) = \frac{1}{n_e} \sum_e l_e * \theta_e \\
\text{Gaussian Curvature:} \quad & K(v) = 2 * \pi - \sum_f \alpha_{f,v}
\end{aligned}
\tag{2.2.1}
$$

where v indicates vertex, f and e are face and edge neighbors of v. $\alpha_{f,v}$ is the angle of face f at v. θ_e is exterior dihedral angle between the two faces intersecting at edge e. n_e and l_e are the number and length of edge e. The Mean curvature is calculated by averaging neighboring edge curvature $H(e) = 2\sin(\theta_e/2) l_e$ (Sullivan, 2008). Because the surface is relatively smooth, the exterior dihedral angle θ_e is usually very small. Then $H(e)$ is approximately equal to $l_e * \theta_e$. A curvature density can be obtained by dividing the curvature by the surface area associated to the vertex v, $A(v) := \frac{1}{3} \sum_f Area(f)$.

2.3   Folding Index

This section follows the anisotropic wavefront propagation method proposed by Lyu et al. (2018). The amount of cortical folding is typically measured within local cortical regions covered by a Euclidean sphere or equidistant geodesic kernel. However, such a kernel may cross several sulci and gyrus. It can smooth out folding details and blurs local gyrification measurements. The anisotropic wavefront propagation can generate a novel kernel shape to quantify cortical gyrification within sulcal and gyral regions locally (Lyu, 2017). The wavefront propagation speed is faster along with the gyral crowns and sulcal fundi.

There are five steps of calculating the folding index.

Step 1: Outer hull creation and correspondence establishment by Laplace and RK4 based streamline computation method. Apply a morphological closing operation to create outer hull. Laplace-PDE solves for a scalar field $u(x)$ between the cortical surface ω and the outer hull surface H.

$$
\begin{aligned}
\nabla^2 u(\mathbf{x}) &= 0 \\
u(\mathbf{x}) &= u_\Omega, \quad \mathbf{x} \in \Omega \\
u(\mathbf{x}) &= u_H, \quad \mathbf{x} \in H
\end{aligned}
\tag{2.3.1}
$$

dl, a differential of length along a streamline, should be parallel to the gradient vector ∇u.

$$
dl \times \nabla u = \left\{ \begin{array}{c} dx \\ dy \\ dz \end{array} \right\} \times \left\{ \begin{array}{c} \frac{\partial u}{\partial x} \\ \frac{\partial u}{\partial y} \\ \frac{\partial u}{\partial z} \end{array} \right\} = \det \begin{vmatrix} \mathbf{i} & \mathbf{j} & \mathbf{k} \\ dx & dy & dz \\ \frac{\partial u}{\partial x} & \frac{\partial u}{\partial y} & \frac{\partial u}{\partial z} \end{vmatrix} = 0 \tag{2.3.2}
$$

Since a mesh is composed of discrete vertices and cells, the PDE can be reduced to an ordinary differential equation (ODE) u_i at any vertex x_i by the method of lines (Schiesser, 2012). Thus, the system of ODEs can be solved by 4th order Runge-Kutta method (Dormand & Prince, 1980).

Step 2: Sulcal and gyral region segmentation via sulcal and gyral curve extraction. Select candidate points that have a maximal negative principal curvature greater than a threshold. Employ the line simplification method to check if points remain after simplification (Ramer, 1972). Connect the neighboring sulcal points with minimal distance along the local principal direction.

Step 3: Cortical region segmentation by computing the geodesic distance between the sulcal and gyral regions. Given a surface ω and its boundary

14

$\partial\omega$, the minimum travel-time $T(x)$ from sources on the boundary to a point x in surface, follows the Eikonal equation, a non-linear partial differential equation encountered in problems of wave propagation (Sethian, 1999).

$$\begin{aligned} \|\nabla T(\mathbf{x})\|F &= 1, \quad \mathbf{x} \in \Omega \subset \mathbb{R}^2 \\ T(\mathbf{x}) &= 0, \qquad \mathbf{x} \in \partial\Omega \end{aligned} \tag{2.3.3}$$

F is the propagation speed. A special form is when $F = 1$, the velocity at any vertex has unit speed, so solution $T(x)$ is equivalent to the geodesic distance (Evans, 1998; Sethian & Popovici, 1999).

Step 4: Compute the principal propagation directions and speeds from the geodesic distance map. A principal propagation direction v_1 is given by the direction of the gradient of the minimum travel-time map. The other principal propagation direction v_2 satisfies $v_1 \perp v_2$. The principal propagation speed along v_1 is maximum, and that along v_2 is minimum, thus yielding a shape-adaptive kernel shape. Linear interpolation gives a normalized travel-time map S. Assigning S and S^{-1} to the speed associated with v_1 and v_2 can guarantee that the amount of propagation is constant as 1.

Step 5: Calculate the folding index using the ratio of areas. A surface is a two-dimensional manifold in a three-dimensional space, so it will be easier to operate only on the manifold. ω can be parametrized to obtain a 2D coordinate system. Since surfaces are represented by vertices and faces, a natural example is to use the row and column

index to encode surface vertices.

Given a small positive value δ, vertex x has a set of neighbor vertices within travel-time δ. The area around x is given by the sum of faces areas containing all neighbor vertices. Thus, we can compute the folding index as the ratio of surface area for Ω and H

$$FI(\mathbf{x};\delta) = \frac{A_\Omega(\mathbf{x};\delta)}{A_H(\mathbf{x};\delta)} \qquad (2.3.4)$$

2.4 Cortical Thickness

The inner and outer surfaces of the cortex have a morphological correspondence. The deformation field can be obtained by non-rigid registration of the inner and outer surface models. Then, the distance that each vertex travels during deformation can be calculated, which is regarded as the cortical thickness. Since the travel path between template vertex and target vertex is a curve, the length of the curve is different from the Euclidean distance between two vertices. Therefore, the cortical thickness calculated in this way is more accurate and reliable.

The registration method used in this section is based on the Large Deformation Diffeomorphic Metric Mapping with imposed normal constraints (Ratnanather et al., 2020).

Thirion (1998) first proposed the diffusion model in which the diffusion equation determines the deformation, together with the Demons algorithm. Later, several studies based on this model and differential manifolds appeared, some of which were combined with other models (Christensen et al., 1996).

16

The diffeomorphic model is based on the mathematical representation of the deformation velocity field. LDDMM registration is a method of locally optimizing the speed of deformation. It generates deformation paths that are not the shortest paths, but paths that minimize the incremental cost of each step. This method has the advantage of solving large deformation problems and is computationally intensive. Since there are large differences between the shapes of the inner and outer cortical surfaces, it is suitable for this method.

A diffeomorphic mapping is smooth and reversible, and the inverse mapping is also smooth. In specific calculations, the Jacobian value of each grid point in the deformation field needs to be greater than zero. It implies a one-to-one and reversible deformation between the inner and outer cortical surfaces. This property ensures that the topology does not change before and after the deformation, including continuity, separability, and smoothness. As a result, more correct correspondences between inner and outer surfaces can be obtained. Some other commonly used algorithms do not guarantee topological correctness, such as the optical flow algorithm (Horn & Schunck, 1981), which may rearrange the brain sulci and gyri and cause errors.

Normal constraints ensure that the velocity field at each vertex is perpendicular to the evolving surfaces. A neuroscience interpretation is that this coordinate system can better mimic the columnar and laminar structure of the cortex.

2.5 Results

Figures 2.5, 2.6, and 2.7 show the 3D cortical surface model and color-coded structural metrics, including curvature, folding index and thickness.
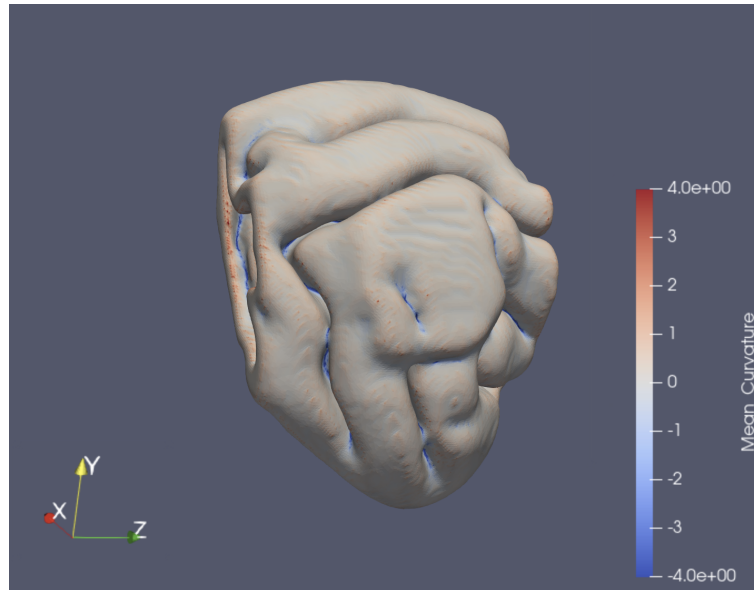
Figure 2.5: Curvature of cat WK7288.

Statistical analysis was performed on all seven subjects. Histograms and Kernel Density Estimate (KDE) plots are shown in figures 2.8,2.9 and 2.10. The density estimator models the probability distribution of the data. The point of highest probability, at the peak of density, is seen as an indicator of the difference between hearing and non-hearing cats. The resampling method can be used to obtain more accurate estimates and measure the degree of uncertainty. Since KDE shape changes as the width and range of bins vary, multiple bin sizes are experimented. After obtaining the highest probability values of each subject, average the values of cats with normal hearing and hearing loss respectively. The results are shown in Table 2.2.
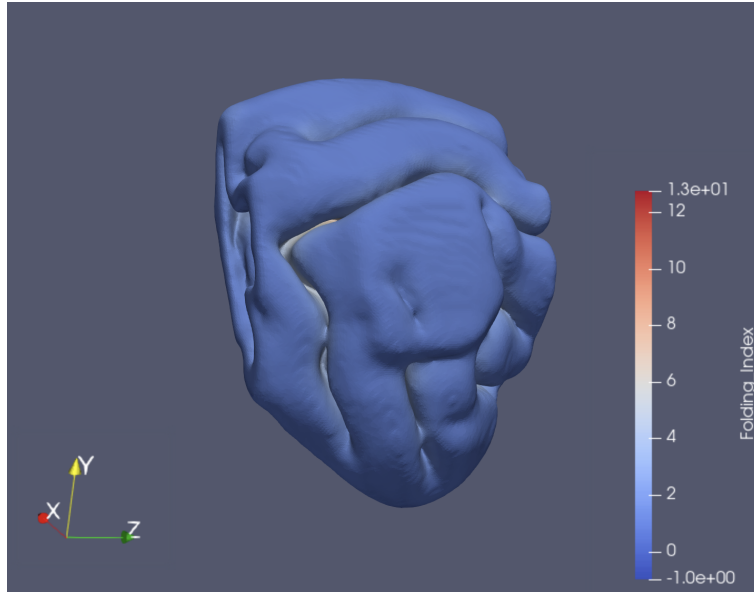
Figure 2.6: Folding index of cat WK7288.
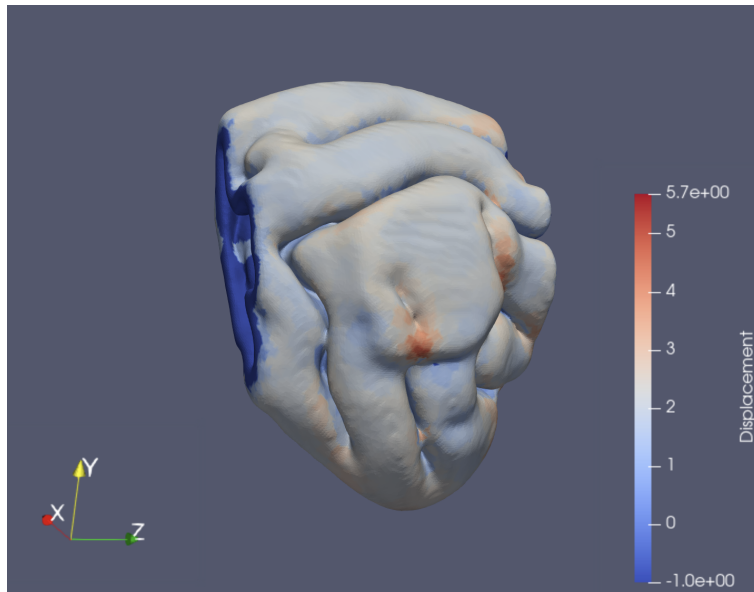
Figure 2.7: Cortical thickness of cat WK7288.

The distributions of curvature are approximately normal distributions. The reason could be that the number of sulci and gyri correspond to each other, resulting in some extent of symmetry in curvature. However, all distributions
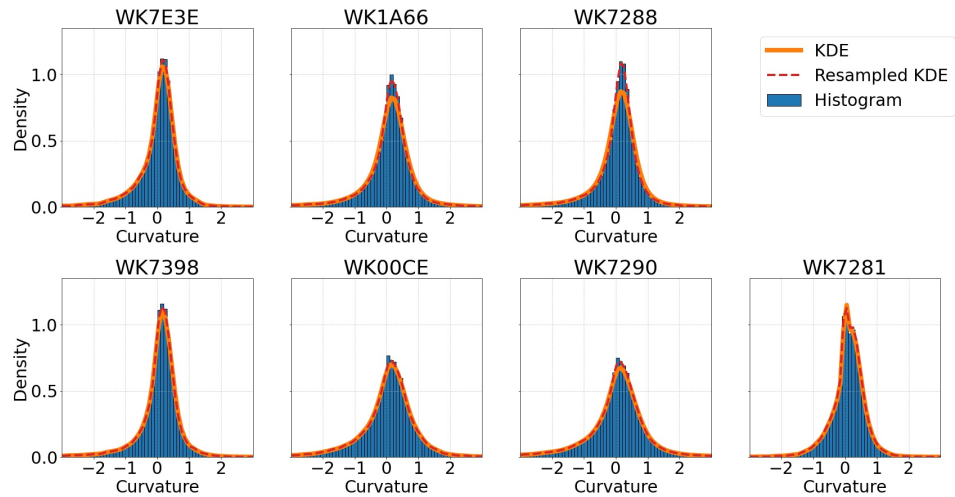
Figure 2.8: Curvature density histogram and KDE plots.
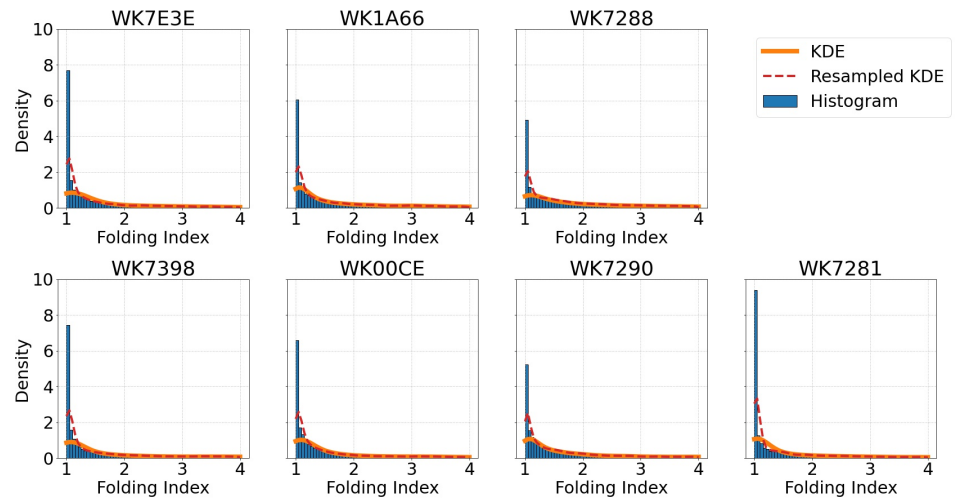
Figure 2.9: Folding index density histogram and KDE plots.

are slightly skewed to the right, indicating that the convex area of the cortical surface is larger than the concave area. All distributions are concentrated around the zero point, implying that most of the cortical surface is relatively
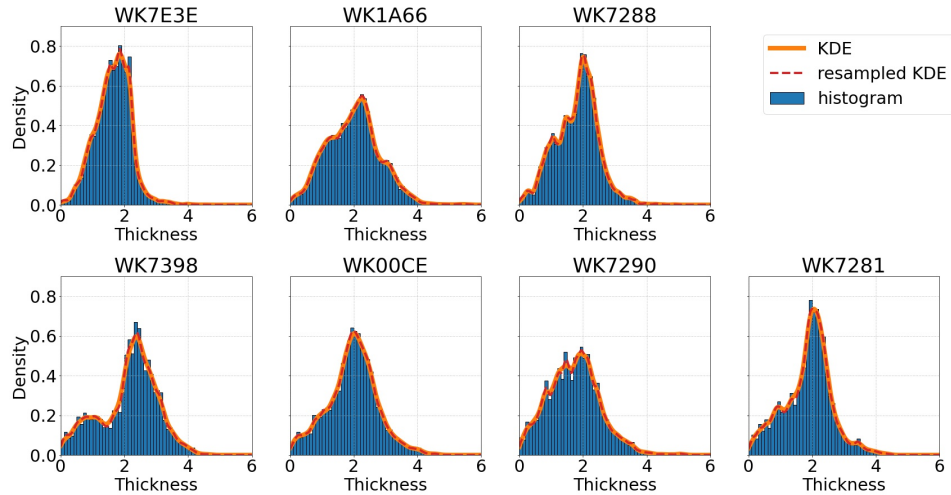
Figure 2.10: Cortical thickness density histogram and KDE plots.

Bin Width	Curvature		Folding Index		Thickness	
	Hearing	HL	Hearing	HL	Hearing	HL
0.1	0.189	0.120	1.094	1.075	2.040	2.093
0.01	0.187	0.120	1.093	1.075	2.037	2.095
0.001	0.189	0.120	1.090	1.076	2.037	2.094

Table 2.2: Average metrics values with the highest probability density of cats with normal hearing and hearing loss(HL). Despite varying bin width, the changes in metrics are consistent. The curvature and folding index of cats with hearing loss are smaller than those of hearing cats, while the thickness increases.

flat. Bilaterally deaf subjects WK00CE and WK7290 have shorter and broader distributions. Left-sided deaf subject WK7281 has a different distribution than others, which appears to have two peaks. The left peak is located at the zero point, indicating WK7281 has more flat regions.

The distributions of folding index are of the same shape, having greatest density at FI = 1. WK7281's distribution has the highest density around FI = 0, which is also related to its large flat regions. Table 2.2 shows that the average

curvature associated with maximum density of non-hearing cats decreases, as well as the folding index. These results suggest that hearing loss is associated with less highly folded cortex.

The distributions of cortical thickness appears to have one to three peaks. Since the data is uneven, it is difficult to identify peaks except for the primary one. Only WK7398's distribution clearly shows two peaks. All distributions have centers in the range of 2.0 and 2.5, and are significantly skewed to the left. It means that thinner parts are larger than thicker parts. Based on observations of color-coded 3D models, such as figure 2.7, gyri are generally thicker than sulci. The observation is consistent with previous research (Holland et al., 2018). According to table 2.2, hearing loss is related with increasing thickness.

Hypothesis testing methods are used to examine the statistical significance of differences between two groups of data. For each cat, 2000 samples are randomly selected. Samples of 3 hearing cats are considered together as the normal hearing group. Samples of 4 hearing loss cats are considered together as the hearing loss group. The most commonly used hypothesis test is the t-test, which usually assumes that the variables have normal distributions (Student, 1908). Welch's t-test is a variation for unequal variances (Welch, 1947). Curvature data is approximately normally distributed. The Welch t-test result of curvature data of two groups shows that $p < 0.01$. Since folding index and thickness data are not normally distributed, the nonparametric Mann-Whitney U (MWU) test is more appropriate (Mann & Whitney, 1947). MWU test result is $p < 0.001$ for both folding index and thickness of two groups. It shows that the metrics distributions have statistically significant differences

between cats with normal hearing and hearing loss.

Chapter 3

Mechanical Model of Cortical Folding

In the previous chapter, cortical morphological metrics of cats with normal hearing and hearing loss were obtained. Observations are that cats with hearing loss have decreased curvature and folding index, and increased thickness. However, it remains unclear what factors contribute to these changes. It is possible that the cortex of cats with hearing loss has different mechanical properties. The influence of mechanical parameters on the folding pattern can be investigated by modeling the brain as a biomechanical model. The modeling results reproduce the cortical folding features obtained in the previous chapter. In that case, the mechanical parameters involved may be relevant to the cause of the abnormal cortical development in cats with hearing loss.

3.1   The Hypothesis of Cortical Folding

Higher primates usually have more complex communication systems. In order to cope with complex environments and cognitive needs, primates need

to incorporate more neurons in a limited space. The cerebral cortex generates sulci and gyri through folding, significantly increasing the number of neurons and bringing them closer to each other. Thus, neurons' communication speed boosts, leading to a greater cognitive information processing speed and better working memory.

There are multiple hypotheses for the mechanism of cortical folding. It was first suggested that the skull may restrict the growth of the brain, leading to compressive stress and flexion (Welker, 1990). Then, it was proposed that axons connecting adjacent areas of the cerebral cortex could pull these areas together (Van Essen, 1997). However, experiments provided evidence against both views (Barron, 1950). Another possible reason is that neurons and glial cells grow in different programmed patterns, expanding more in some areas than others (Kriegstein et al., 2006; Reillo et al., 2011). However, there is evidence that the folded cortex pulls on the underlying tissue, not the underlying tissue pushes outward on the cortex and force it to fold (Xu et al., 2010). Therefore, the neurons and glial cells differences may have affected only the early stage of primary folding.

In recent years, a popular hypothesis is the tangential expansion hypothesis based on the different properties of gray and white matter (Richman et al., 1975). The tangential expansion of the outer region is larger than that of the inner region and causes folding through mechanical instability. Many studies are based on this hypothesis because it can be modeled both in vivo and numerically (Bayly et al., 2013; Dervaux & Amar, 2008; Tallinen et al., 2014; Tallinen et al., 2016). This chapter uses such a finite element model to study

the effect of different shear modulus and bulk modulus of gray and white matter on the folding of the cortex.

3.2 Model
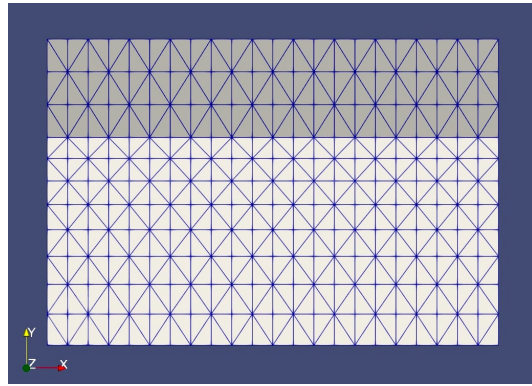
Figure 3.1: An example of 2D mechanical model. The upper region represents the gray matter, while the lower region represents the white matter.

The finite element model consists of a uniform triangular mesh, as shown in figure 3.1. It has two components, an upper component representing the gray matter and a lower component representing the white matter. The upper component has a tangential expansion parallel to the tangent of the surface. The white matter does not expand on its own, but deforms together with the gray matter due to elastic forces. The model material is Neo-Hookean solid with compressible hyper-elastic property. The neo-Hookean energy-density function models nonlinear elasticity.

Consider a displacement field $u_i(x_j)$. The deformation gradient is

$$F_{ij} = \delta_{ij} + \frac{\partial u_i}{\partial x_j} \tag{3.2.1}$$

Let B denote the left Cauchy-Green deformation tensor,

$$B = F \cdot F^T, \quad B_{ij} = F_{ik}F_{jk} \tag{3.2.2}$$

There are several invariants of B, including

$$\bar{I}_1 = \frac{\text{tr}(B)}{J^{2/3}}; \quad J = \sqrt{\det(B)} \tag{3.2.3}$$

The stress-strain relation follows as

$$\sigma_{ij} = \frac{\mu}{J^{5/3}} \left(B_{ij} - \frac{1}{3}B_{kk}\delta_{ij} \right) + K(J-1)\delta_{ij} \tag{3.2.4}$$

where μ is the shear modulus, K is the bulk modulus.

The corresponding strain energy density is

$$\bar{U} = \frac{\mu}{2}(\bar{I}_1 - 3) + \frac{K}{2}(J-1)^2 \tag{3.2.5}$$

The cortical tissue is assumed to be incompressible. To limit compressibility, K must be much larger than μ. Here we set $K = 10^3\mu$. In the finite element model, each vertex has its own value of shear modulus, bulk modulus and growth. In each iteration, the Cauchy stress is calculated by equation 3.2.4. The force on each triangle is evenly distributed to the three vertices. Based on quasi-static approximation, the energy of system needs to be minimized at each step. It means that the system changes so slow that after every step, it reaches a new equilibrium. The equations are as follows.

$$\begin{aligned} \Delta v_i &= \frac{F_i - v_i * \gamma}{a} * \Delta t \\ \Delta u_i &= v_i * \Delta t \end{aligned} \tag{3.2.6}$$

where a is the volume occupied by a vertex, γ is the damping factor.

The finite element model of high-density mesh has high computational complexity. Assuming the model is symmetric, it can be seamlessly connected by translation, allowing faster computation. Boundary conditions are added to the edge vertices of the model: the corresponding starting and ending vertices have the same forces and velocities.

It needs to be ensured that the surface of the model does not intersect. That is, the surfaces on both sides of a sulcus during folding will stop growing after contacting each other because of squeezing. Since the vertices under the top surface will not pass the vertices on the surface, only the repulsive forces between the vertices and triangles on the surface need to be calculated. In each iteration, search for the neighboring triangles within a specific range of each vertex. If the distance between a vertex v and a neighboring triangle f is smaller than a threshold value, a repulsive force will be applied to v. Based on the relative position of v to f, add a repulsive force in the opposite direction to f's vertices in a calculated proportion.

In order to better mimic gray matter and white matter, the thickness of the lower region is considerably thicker than the upper one. However, folding occurs mainly in the upper region, while the bottom part remains almost unchanged. Therefore, the height of each row in the lower region is increased exponentially to reduce mesh density and improve computational speed, as shown in figure 3.1.

The model has 2D and 3D versions. In 2D model, the gray matter grows only in x-direction. In 3D model, the gray matter grows in x- and z-direction.

Among all the biomechanical parameters related with cortical folding, the most critical ones are shear modulus and bulk modulus. Shear modulus indicates the rigidity of an object. If a force is applied to the surface of an object parallel to the surface, the surface of the object will be pushed to one side, producing an angular deformation. The smaller the shear modulus, the softer the object and the easier it is to deform. Bulk modulus, also known as incompressibility, is the ratio between the increase in force and the resulting decrease in volume of the object. The smaller the bulk modulus, the more easily an object can be compressed.

In the numerical experiments, the model's initial shear modulus is 1.0, and the bulk modulus is 1000 times the shear modulus. We have explored values that reduce or increase the modulus of gray matter or white matter within the central area or all areas. Then, the curvature, folding index, and cortical thickness of the 2D and 3D model folding results are investigated based on the methods described in the previous chapter. The calculation is simplified because the model already gives the deformation field and the correspondence between vertices.

The simulation code is adapted from Tallinen's source code of soft matter mechanics numerical models (Tallinen et al., 2014). Input parameters include the length and number of vertices in each direction, total simulation time, time step, auto-save interval, initial shear modulus and bulk modulus. For different settings, the code finds the index of vertices in the region of interest (ROI) based on position, and assigns them a different modulus. There are three presets of ROI, the lower region, the center of the lower region, and

the center of both regions. When starting the simulation, input includes the number of preset and the modified modulus. During simulation, at the set interval, data containing structure and stress information is output to a result folder in POV-Ray format (Persistence of Vision Pty. Ltd.). After simulation, POV-Ray-based images and VTK files of multiple models at desired timestep are generated in batch.

3.3 Results of 2D Models
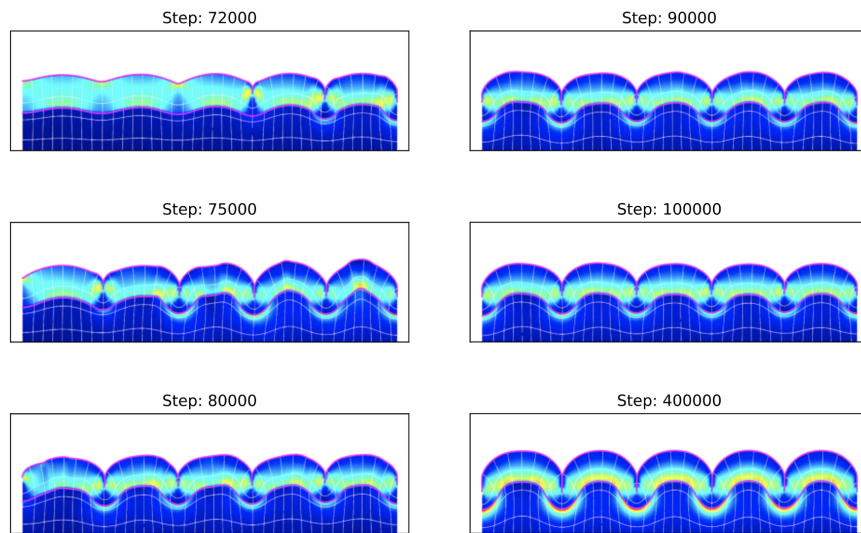
Figure 3.2: Folding progress of the initial model from time step 72000 to 400000. Shear modulus is 1.0; Bulk modulus is 1000.0. The boundary of the upper region is labeled in pink. Green, yellow and red indicate increasing stress. The model first forms a shallow sulcus on the right side, then spreads out to the left and right. Finally, a periodic wave-shaped folding pattern is generated.

The folding progress of the initial model is shown in figure 3.2. After generating a stable wave-shaped periodic folding pattern, the upper region grows in the y-direction and increases the amplitude, while its wavelength

remains unchanged. This is consistent with previous research, indicating that there is an optimum wavenumber that minimizes the total free energy, which is proportional to the initial thickness (Groenewold, 2001). Figure 3.3 shows that the thickness of gyri is larger than that of sulci, consistent with previous observations in computational simulations, polymer experiments, and the human brain (Holland et al., 2018).
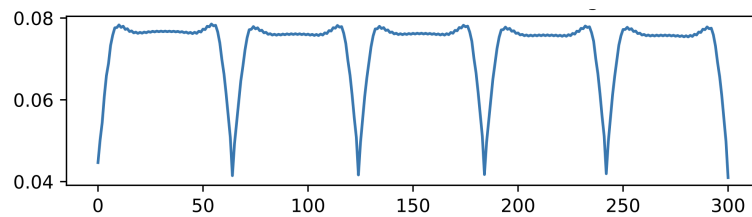
Figure 3.3: Cortical thickness of the initial model at time step 400000. The minimum thickness is 0.04097. The max thickness is 0.07854. The average value is 0.07301. Since the model has no actual physical sizes, all variables can be linearly transformed in the same scale. Therefore, there is no need for units of variables and metrics.

There are two types of variations to the initial model with a shear modulus of 1.0.

1. Change the shear modulus to 0.8, 0.9, 1.1, or 1.2. Bulk modulus is set to 1000.0 times shear modulus.

2. Change the region of modifying shear modulus. The region can be the whole lower region, the center of both regions, and the center of the lower region.

By combining the two variations, various parameter settings can be obtained. Changing the modulus of the entire lower region mainly affects the number and length of cycles. For example, increasing it from 1.0 to 1.2 results
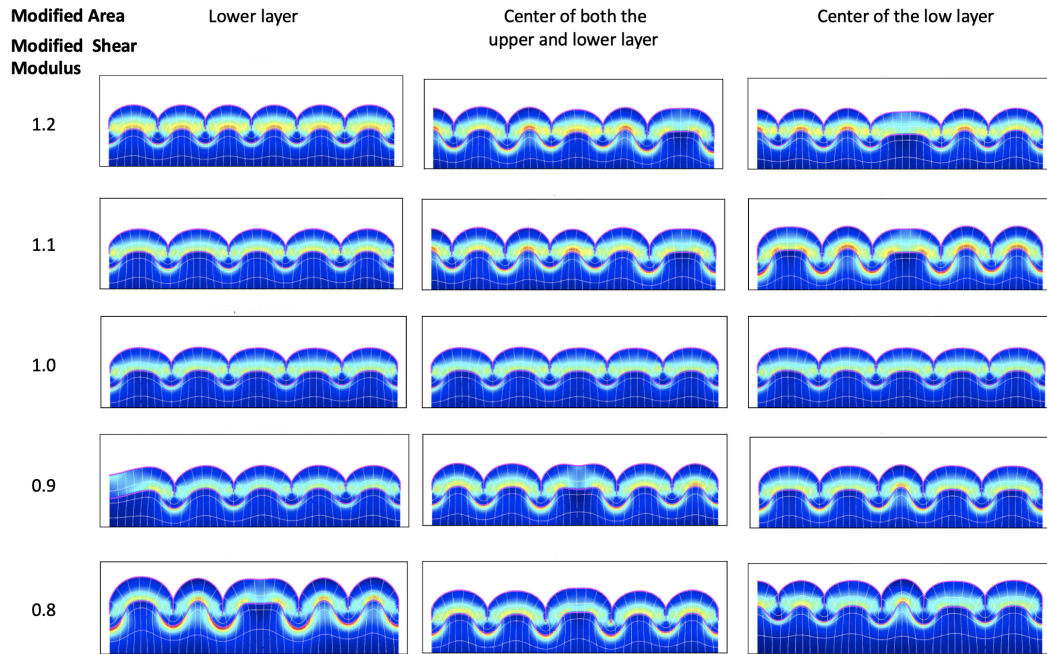
Figure 3.4: Stable folding patterns of various modulus settings. Different models reach a relatively stable state at different times, depending on their mechanical properties.

in an increased periodic number, from 5 to 6. Models with decreased modulus in the central part of both regions will form the first gyrus at the center, because a small modulus means that the material is easy to deform. This first gyrus is formed earlier and thus squeezed by both sides to develop into a narrowed gyrus.

Changing only the central lower region will result in regularity. If the modulus is increased, the model will form a wide central gyrus. If the modulus is decreased, the model will form a narrow central gyrus. This is because the area with a large modulus is more difficult to deform and curve. The width of the central gyrus is positively correlated with the modulus being altered. In addition, the cortical thickness decreases as the modulus rises, as shown in

figure .

3.4   Results of 3D Models

Figure 3.6, 3.7, 3.8, and 3.9 show the results of modifying the modulus in the center of both regions or only lower region of 3D models. The density histograms of center vertices and non-center vertices are labeled red and yellow respectively. Values with the highest probability are calculated based on KDE and plotted in figure 3.10.

As the modulus increases, the difference of curvature distribution between
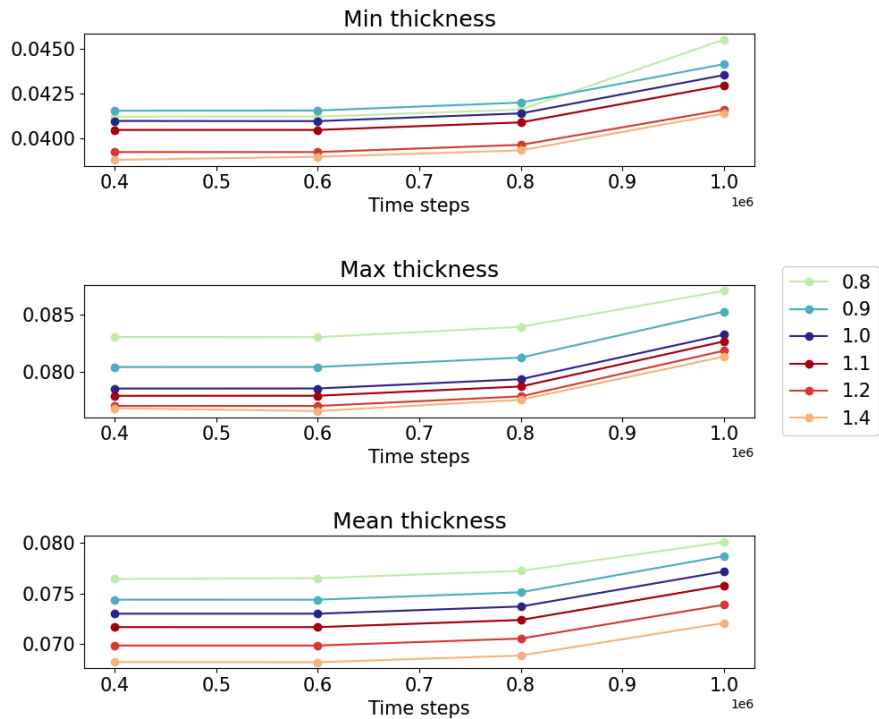
Figure 3.5: Thickness of models varying the modulus of central lower region. The minimum, maximum, and average thickness all have a positive correlation with the changes modulus.
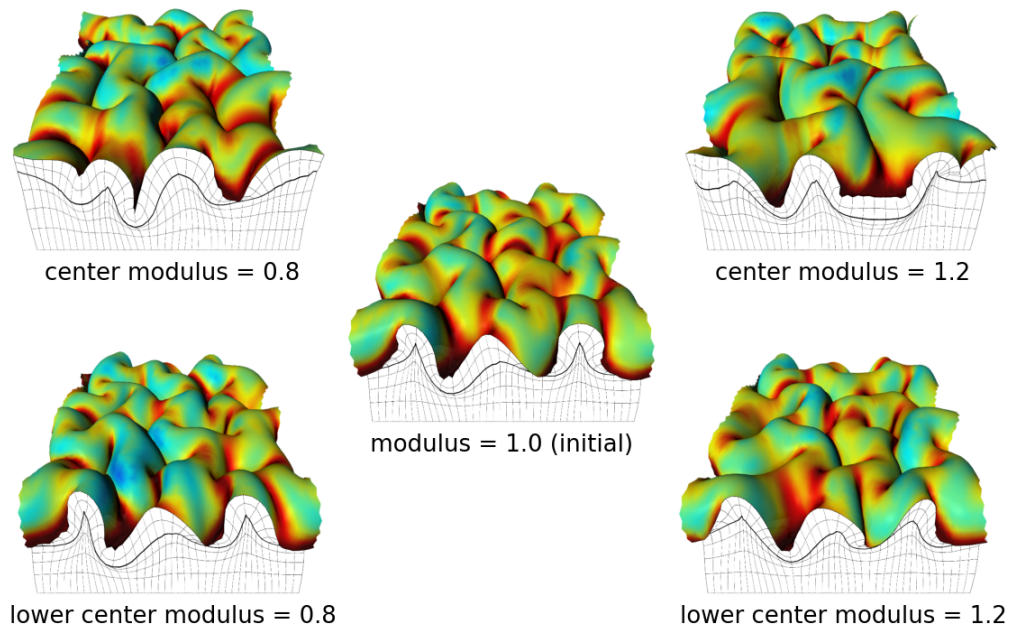
Figure 3.6: Folding results of 3D models. Stress is color-coded. When modulus is decreased, the surface is more highly folded, and the sulci grow deeper.

center and noncenter vertices increases. The curvature of center vertices shows a positive correlation with modulus, while that of noncenter vertices shows a negative correlation. It suggests that the spatial inhomogeneity of modulus cause different sharpness of folds in different areas, and a higher center modulus may enlarge this difference.

In figure 3.10b, folding index fluctuates around a downward trend as modulus increases. The downward trend is consistent with the fact that a large modulus results in difficulty to deform.

When changing the modulus of the center lower region, the thickness is positively correlated with the modulus. The thickness of center vertices becomes greater than that of noncenter vertices as modulus increase, and
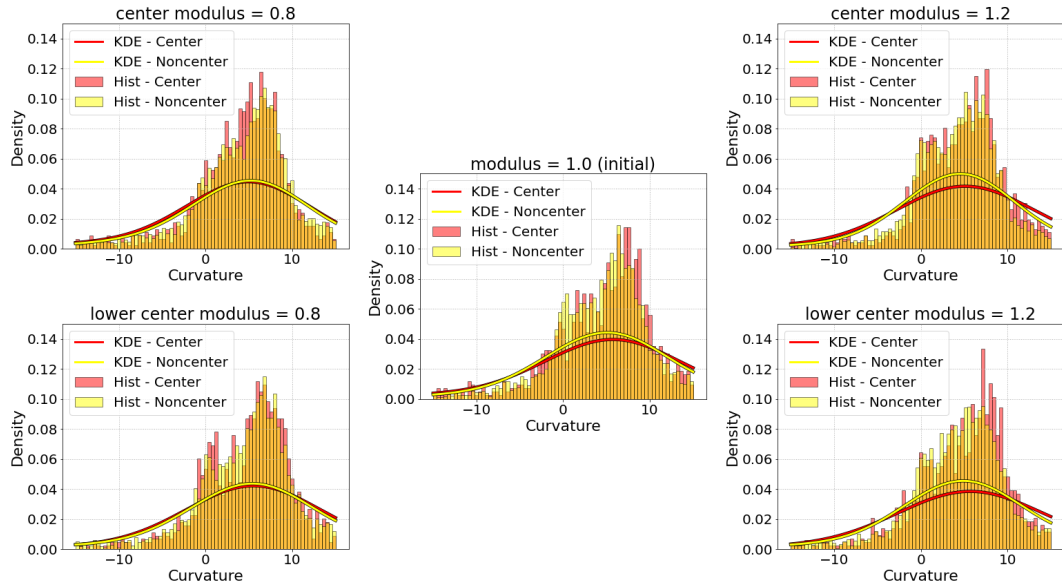
Figure 3.7: Density histogram and KDE plot for curvature of 3D models.
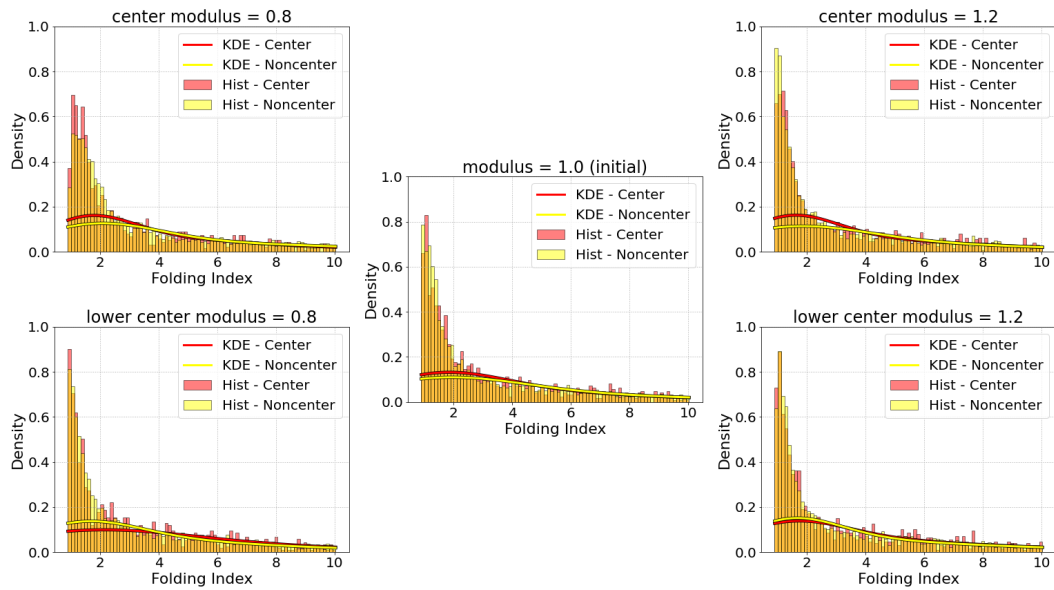
Figure 3.8: Density histogram and KDE plot for curvature of 3D models.
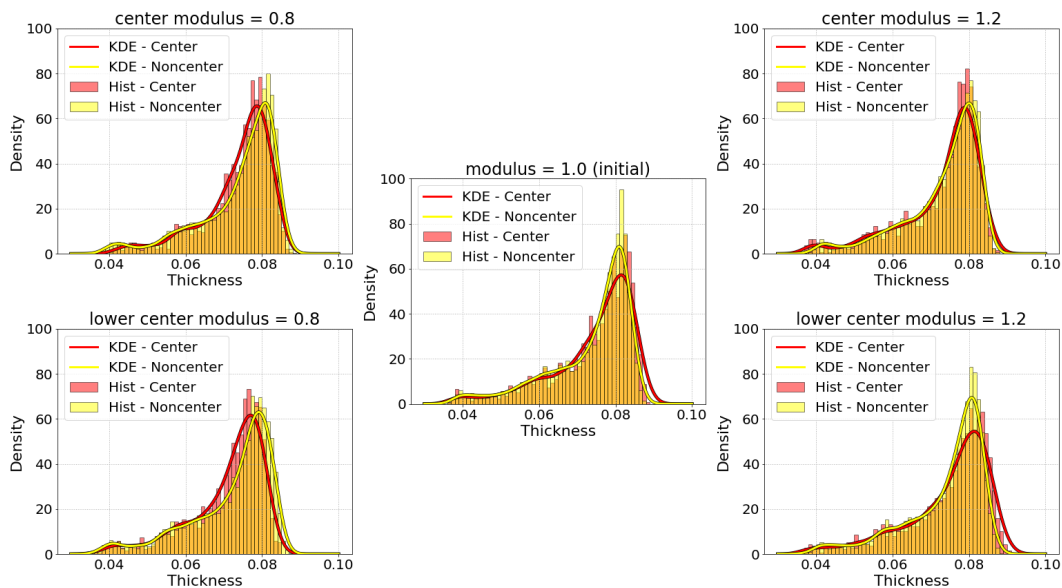
Figure 3.9: Density histogram and KDE plot for curvature of 3D models.

smaller as modulus decrease. The upward trend of average thickness is consistent with 2D simulations. When changing both regions, the thickness of center vertices decreases in both directions of modulus varied from the initial value of 1.0.
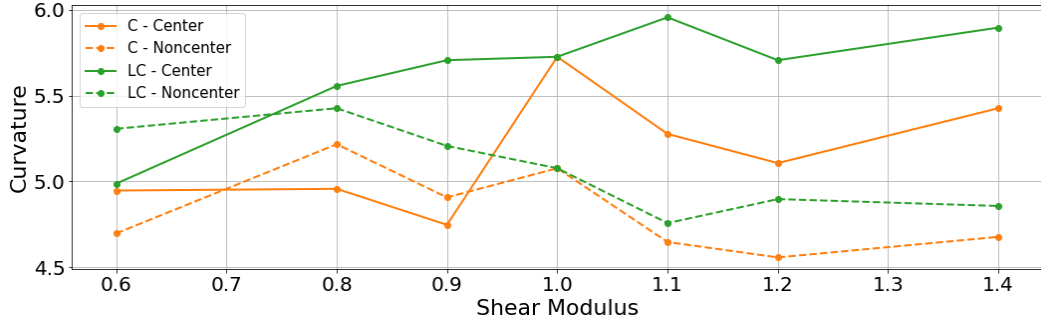
(a) Curvature
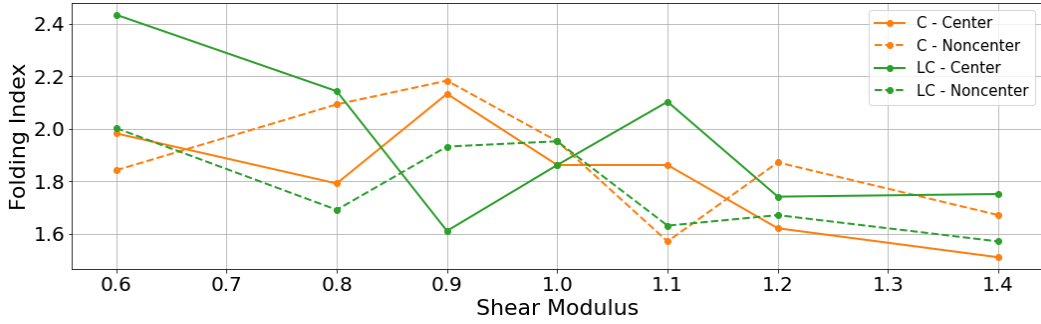
(b) Folding Index
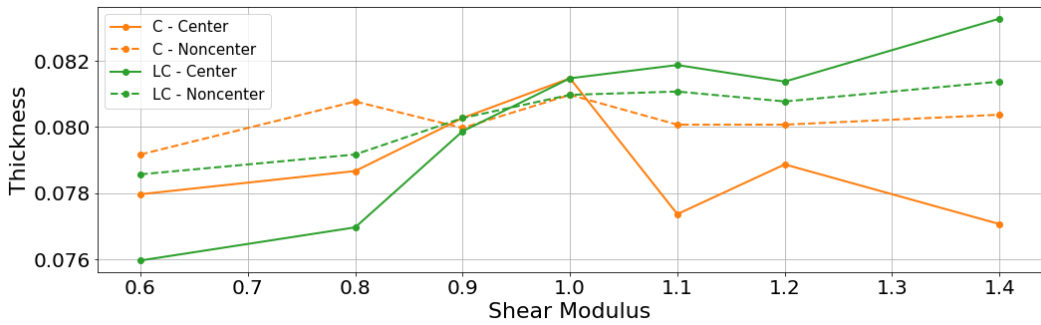
(c) Thickness

Figure 3.10: Metrics values with the highest probability density. C (orange) means modifying the center modulus of both regions. LC (green) means modifying the center modulus of lower region. Center (solid line) labels the vertices whose modulus is changed, and Noncenter (dash line) labels the unchanged vertices.

Chapter 4

Discussion

4.1 Discussion

The first part of this work proposes a pipeline for automatically measuring cortical morphological metrics based on MRI images, and statistically analyzes the results of hearing cats and non-hearing cats. By automatically preprocessing MRI images, including extracting 3D surface models from segmentation and separating the inner and outer surfaces, manual work can be saved. It can speed up data processing and support brain morphology research. The second part uses a finite element mechanical model to simulate cortical folding and study the influence of different biomechanical parameters on folding patterns. The 3D model can directly use the mentioned pipeline to calculate metrics and perform statistical analysis. This framework can also be extended for many other neural disorders or brain development researches.

Data analysis based on MRI images showed that, compared with hearing cats, the average curvature and folding index of cats with hearing loss decreased, while the thickness increased. In the experiments of 2D mechanical

models, increasing the shear modulus and bulk modulus in the central white matter region can lead to the formation of a wider and flatter gyrus. Reducing the modulus of the central white matter region or both regions can result in an increased thickness. However, raising the modulus of the entire white matter region can also result in an increased thickness. In 2D and 3D models, reducing the modulus of the center of both regions will result in a larger maximum thickness. These results seem to be contradictory and need to be discussed.

First, increasing the modulus of the entire white matter region will not change the uniform waveform folding pattern, but will affect the periodic length and number. Because the modulus of gray matter does not change, the surface grows outwards. The white matter is difficult to deform, so the thickness increases until the elasticity is enough to force the white matter to deform and fold. At this time, the thickness was already very large. The greater the modulus, the greater amount of gray matter's deformation is required, resulting in greater thickness.

Mechanical modeling results provide evidence that folding can inhibit thickness growth. In the early stages of folding, a gyrus and two sulci form, and this region is thinner than flat areas. It may be because the cortex grows in the tangential direction, but it is squeezed to grow in the surface normal direction. If the region's modulus is small and is easy to fold, it only needs to grow and fold along the surfaces, so the stress and the growth in the surface normal direction are reduced. There may even be an opposite force causing the thickness to decrease. In addition, the thickness of a sulcus itself is smaller

than that of flat areas, which affects the average thickness.

Reducing the modulus of the central white matter region can also increase the thickness. If the modulus of the central white matter region is reduced in the experiments, the model will first form a gyrus and two sulci in the center. The smaller the modulus, the narrower the central gyrus. Since white matter is more easily deformed than gray matter, these two sulci will grow deeper, while the width of the gyrus is almost unchanged. Therefore, the central part mainly undertakes the pressure of tangential growth. The side parts do not fold in the early stage. They grow outwards, increasing the thickness of the grey matter region. After that, the pressure spreads from the center to the sides, and the sides begin to fold. The lower the modulus is, the slower the propagation speed of folding, the more that sides can grow outward, resulting in larger maximum thickness and average thickness. If the modulus is large than the initial values, the deep brain sulcus is formed on the sides, the center area becomes flatter and thicker than the sides. The greater the modulus, the faster the folding propagates to the center, and the smaller the thickness of the center area can reach in the early stage.

If change the modulus of the center of both regions, the effect is similar to that of only changing the white matter region, but it did not show much regularity. Generally, when the modulus is reduced, the central gyrus of the former is narrower, the fold spreads faster, and the maximum and average thickness are larger. When the modulus is increased, the central gyrus becomes wider and flatter, and the maximum thickness is larger, while the average thickness is almost equal. These results imply that the different properties of

gray matter and white matter will influence the cortical folding pattern.

When reducing the modulus of the entire white matter region, the smaller the modulus, the larger the absolute average curvature value, which is negative. It is probably because objects with small modulus are easy to deform, fold and form brain sulci. When changing the modulus of the central white matter region, the greater the modulus, the greater the average folding index. When changing the modulus of the entire white matter region, the average folding index increases as the modulus decreases.

The mechanical properties of brain tissue depend on its histological composition and structure. The gray matter consists of neuronal cell bodies, glial cells, unmyelinated axons, and capillaries. The white matter consists mainly of myelinated axons (Purves et al., 2008). Several studies have found gray matter to be more rigid than white matter (Budday et al., 2017; Green et al., 2008), but there is also evidence against this conclusion (Kruse et al., 2008; McCracken et al., 2005; Velardi et al., 2006). Budday et al. (2017) shows that white matter is not significantly anisotropic, even though the distribution of nerve fibers can be highly anisotropic. Some studies observed more stiffness along the fiber direction than in the perpendicular direction (Feng et al., 2013; Jin et al., 2013; Velardi et al., 2006; Yousefsani et al., 2018), but others have suggested otherwise (Budday et al., 2017; Prange & Margulies, 2002). A simulation study found stress concentrations near small axons when fiber diameters are different (Yousefsani et al., 2018).

Studies have shown that auditory deprivation affects the development of myelin in the cortex (Kohrman et al., 2021; Long et al., 2018). Myelin promotes

the speed of neuronal communication and is therefore essential for auditory function. Primates are born with almost no myelin in the auditory cortex and reach the highest amount of myelin after adulthood (Miller et al., 2013). Myelin has plasticity, so its development will be affected by experience deprivation, including social activity, vision, tactile and auditory experiences (Barrera et al., 2013; Etxeberria et al., 2016; Hribar et al., 2014; Makinodan et al., 2012; Smith et al., 2011). Studies based on Magnetic Resonance Elastography and Atomic Force Microscopy found that demyelination decreases shear modulus (Heredia et al., 2007; Schregel et al., 2012). Therefore, auditory deprivation may result in reduced myelin formation in the white matter and thus reduced modulus.

Auditory deprivation can also reduce dendritic tree size or density and number of neurons (Bose et al., 2010; Gröschel et al., 2010; Klinke et al., 1999; McMullen et al., 1988; Ouda et al., 2016). Clemo et al. (2017) found significantly increased spine density in the supragranular layers of deaf cats, and significantly decreased spine density of spiny non-pyramidal neurons in the granular layer. They also found that spine head diameter was significantly increased in the supragranular layers, and decreased in the infragranular layers. The increased density may be related to reduced synaptic pruning affected by experience deprivation (Cardon et al., 2012; Jiang et al., 2009). Yang et al. (2020) found that the average elastic modulus of spines was much larger than that of gray matter and white matter, and it had no significant correlation with spine size. It suggests that the overall modulus may increase with increasing spine density. Thus, auditory deprivation may increase the

modulus in supragranular layers and decrease that in granular layers.

In addition to neuron and fiber, interconnections and capillary density also affect brain tissue stiffness (Budday et al., 2017). Additionally, Sunnerberg et al. (2019) demonstrated a negative correlation between cell volume and modulus.

4.2 Limitations and Future Work

A major limitation is the impact of the limited spatial resolution of MRI on cortex segmentation. If the two sides of a brain sulcus are close to each other, accurate segmentation is not guaranteed even with manual editing. An improvement idea is to involve histological brain slice imaging for multimodal surface reconstruction (Ewert et al., 2018; Mancini et al., 2020). Although histological optical imaging is usually in vitro or invasive, it allows for the best spatial resolution and thus a more precise segmentation. Registering histological images to MRI images of the same subject can repair the distortions of brain slices. In addition to the binary cortical segmentation, brain regions can be labeled using these high-resolution images. Brain-region-specific statistical analysis of data can help to measure the structural metrics for interested regions and better understand the relationship between regions.

The mechanical cortex model used in this work is only a simplified model with few mechanical properties and basic shapes. A model of primary cortical folding can be obtained by smoothing out the highly-folded features of the surface model extracted from MRI. Assigning mechanical properties to a three-dimensional model like an embryonic brain may allow a more realistic

imitation of the higher-order folding process of the cortex. It can help with investigating the effect of different biomechanical parameters in brain development. Moreover, the model in this work has only two components, mimicking the gray and white matter. It will be helpful to study the role of different cortical layers by adding more components to the model. Also, the cellular and molecular mechanisms of cortical enlargement, thickening, and folding have been examined (Liu et al., 2017). The programmed growth pattern of neurons and other cells can be relevant to cortical folding. A possible research direction is to combine cellular mechanisms with finite element models and add more anisotropic biomechanical parameters to mimic cells' behaviors.

Appendix A

Software and Data

A.1   Software

Description	Location
Instructions of cortical morphology analysis and mechanical modeling	/cis/project/deafcat/mri/cortmorph/README.md, /cis/project/deafcat/mri/mechmodel/README.md
Convert segmentation to surface - Delaunay Triangulation	/cis/project/deafcat/mri/cortmorph/daniel/seg2Surf/ seg2Surf.m
Convert segmentation to surface - Marching Cubes	/cis/project/deafcat/mri/cortmorph/vtkUtils/volume2vtk.m
Separate the outer and inner cortical surfaces - automatically	/cis/project/deafcat/mri/cortmorph/vtkUtils/surface_cut.py
Separate the outer and inner cortical surfaces - manually	/cis/project/deafcat/mri/cortmorph/conniejhe/Surface-Cutting/
Calculate curvature	/cis/project/deafcat/mri/cortmorph/vtkUtils/curv.py
Calculate folding index	/cis/project/deafcat/mri/cortmorph/LocalGyrificationIndex/
Calculate thickness	/cis/project/deafcat/mri/cortmorph/registration/
Register histology images to MRI images	/cis/project/deafcat/mri/cortmorph/his2mri/
Operate VTK files - smooth, reduce the number of vertices, subdivide, convert other formats to VTK, etc.	/cis/project/deafcat/mri/cortmorph/vtkUtils/
2D mechanical model - simulation and analysis	/cis/project/deafcat/mri/mechmodel/2d/code
3D mechanical model - simulation and analysis	/cis/project/deafcat/mri/mechmodel/3d/code

Table A.1: Software locations.

A.2 Data

Description	Location
Cat MRI and segmentations	/cis/project/deafcat/mri/Cats_data/mriSeg/
Surface models with curvature, folding index and thickness data	/cis/project/deafcat/mri/Cats_data/results/
2D mechanical model - simulation and analysis results	/cis/project/deafcat/mri/mechmodel/2d/results, /cis/project/deafcat/mri/mechmodel/2d/analysis
3D mechanical model - simulation and analysis results	/cis/project/deafcat/mri/mechmodel/3d/results, /cis/project/deafcat/mri/mechmodel/3d/analysis

Table A.2: Data locations.

References

Barrera, K., Chu, P., Abramowitz, J., Steger, R., Ramos, R. L., & Brumberg, J. C. (2013). Organization of myelin in the mouse somatosensory barrel cortex and the effects of sensory deprivation. *Developmental neurobiology*, *73*(4), 297–314.

Barron, D. H. (1950). An experimental analysis of some factors involved in the development of the fissure pattern of the cerebral cortex. *Journal of Experimental Zoology*, *113*(3), 553–581.

Bayly, P., Okamoto, R., Xu, G, Shi, Y, & Taber, L. (2013). A cortical folding model incorporating stress-dependent growth explains gyral wavelengths and stress patterns in the developing brain. *Physical biology*, *10*(1), 016005.

Bergsma, D. R., & Brown, K. S. (1971). White fur, blue eyes, and deafness in the domestic cat. *Journal of Heredity*, *62*(3), 171–183.

Bok, S. T. (1959). *Histonomy of the cerebral cortex*. Elsevier Publishing Company.

Bose, M., Muñoz-llancao, P., Roychowdhury, S., Nichols, J. A., Jakkamsetti, V., Porter, B., Byrapureddy, R., Salgado, H., Kilgard, M. P., Aboitiz, F., et al. (2010). Effect of the environment on the dendritic morphology of the rat auditory cortex. *Synapse*, *64*(2), 97–110.

Bradski, G. (2000). The OpenCV Library. *Dr. Dobb's Journal of Software Tools*.

Budday, S., Nay, R., de Rooij, R., Steinmann, P., Wyrobek, T., Ovaert, T. C., & Kuhl, E. (2015). Mechanical properties of gray and white matter brain tissue by indentation. *Journal of the mechanical behavior of biomedical materials*, *46*, 318–330.

Budday, S., Sommer, G., Birkl, C., Langkammer, C., Haybaeck, J., Kohnert, J., Bauer, M., Paulsen, F., Steinmann, P., Kuhl, E., et al. (2017). Mechanical characterization of human brain tissue. *Acta biomaterialia*, *48*, 319–340.

Budday, S., & Steinmann, P. (2018). On the influence of inhomogeneous stiffness and growth on mechanical instabilities in the developing brain. *International Journal of Solids and Structures*, *132*, 31–41.

Butler, B. E., & Lomber, S. G. (2013). Functional and structural changes throughout the auditory system following congenital and early-onset deafness: Implications for hearing restoration. *Frontiers in systems neuroscience*, *7*, 92.

Cardon, G., Campbell, J., & Sharma, A. (2012). Plasticity in the developing auditory cortex: Evidence from children with sensorineural hearing loss and auditory neuropathy spectrum disorder. *Journal of the American Academy of Audiology*, *23*(6), 396–411.

Chew, L. P. (1989). Constrained delaunay triangulations. *Algorithmica*, *4*(1), 97–108.

Christensen, G. E., Rabbitt, R. D., & Miller, M. I. (1996). Deformable templates using large deformation kinematics. *IEEE transactions on image processing*, *5*(10), 1435–1447.

Clemo, H. R., Lomber, S. G., & Meredith, M. A. (2017). Synaptic distribution and plasticity in primary auditory cortex (a1) exhibits laminar and cell-specific changes in the deaf. *Hearing research*, *353*, 122–134.

da Costa Campos, L., Hornung, R., Gompper, G., Elgeti, J., & Caspers, S. (2021). The role of thickness inhomogeneities in hierarchical cortical folding. *NeuroImage*, *231*, 117779.

Das, S. R., Avants, B. B., Grossman, M., & Gee, J. C. (2009). Registration based cortical thickness measurement. *Neuroimage*, *45*(3), 867–879.

Dervaux, J., & Amar, M. B. (2008). Morphogenesis of growing soft tissues. *Physical review letters*, *101*(6), 068101.

Dijkstra, E. W. et al. (1959). A note on two problems in connexion with graphs. *Numerische mathematik*, *1*(1), 269–271.

Dormand, J. R., & Prince, P. J. (1980). A family of embedded runge-kutta formulae. *Journal of computational and applied mathematics*, *6*(1), 19–26.

Etxeberria, A., Hokanson, K. C., Dao, D. Q., Mayoral, S. R., Mei, F., Redmond, S. A., Ullian, E. M., & Chan, J. R. (2016). Dynamic modulation of myelination in response to visual stimuli alters optic nerve conduction velocity. *Journal of Neuroscience*, *36*(26), 6937–6948.

Evans, L. C. (1998). Partial differential equations. *Graduate studies in mathematics*, *19*(2).

Ewert, S., Plettig, P., Li, N., Chakravarty, M. M., Collins, D. L., Herrington, T. M., Kühn, A. A., & Horn, A. (2018). Toward defining deep brain stimulation targets in mni space: A subcortical atlas based on multimodal mri, histology and structural connectivity. *Neuroimage*, *170*, 271–282.

Fedorov, A., Beichel, R., Kalpathy-Cramer, J., Finet, J., Fillion-Robin, J.-C., Pujol, S., Bauer, C., Jennings, D., Fennessy, F., Sonka, M., et al. (2012). 3d slicer as an image computing platform for the quantitative imaging network. *Magnetic resonance imaging*, *30*(9), 1323–1341. https://www.slicer.org/

Feng, G., Ingvalson, E. M., Grieco-Calub, T. M., Roberts, M. Y., Ryan, M. E., Birmingham, P., Burrowes, D., Young, N. M., & Wong, P. C. (2018). Neural preservation underlies speech improvement from auditory deprivation in young cochlear implant recipients. *Proceedings of the National Academy of Sciences*, *115*(5), E1022–E1031.

Feng, Y., Okamoto, R. J., Namani, R., Genin, G. M., & Bayly, P. V. (2013). Measurements of mechanical anisotropy in brain tissue and implications for transversely isotropic material models of white matter. *Journal of the mechanical behavior of biomedical materials*, *23*, 117–132.

Garcia, K., Kroenke, C., & Bayly, P. (2018). Mechanics of cortical folding: Stress, growth and stability. *Philosophical Transactions of the Royal Society B: Biological Sciences*, *373*(1759), 20170321.

Gautam, P., Anstey, K. J., Wen, W., Sachdev, P. S., & Cherbuin, N. (2015). Cortical gyrification and its relationships with cortical volume, cortical thickness, and cognitive performance in healthy mid-life adults. *Behavioural brain research*, *287*, 331–339.

Green, M. A., Bilston, L. E., & Sinkus, R. (2008). In vivo brain viscoelastic properties measured by magnetic resonance elastography. *NMR in Biomedicine: An International Journal Devoted to the Development and Application of Magnetic Resonance In vivo*, *21*(7), 755–764.

Groenewold, J. (2001). Wrinkling of plates coupled with soft elastic media. *Physica A: Statistical Mechanics and its Applications*, *298*(1-2), 32–45.

Gröschel, M., Götze, R., Ernst, A., & Basta, D. (2010). Differential impact of temporary and permanent noise-induced hearing loss on neuronal cell density in the mouse central auditory pathway. *Journal of neurotrauma*, *27*(8), 1499–1507.

Hansen, G., Crooks, L. E., Davis, P., De Groot, J, Herfkens, R, Margulis, A., Gooding, C, Kaufman, L, Hoenninger, J, Arakawa, M, et al. (1980). In vivo imaging of the rat anatomy with nuclear magnetic resonance. *Radiology*, *136*(3), 695–700.

Heid, S., Hartmann, R., & Klinke, R. (1998). A model for prelingual deafness, the congenitally deaf white cat–population statistics and degenerative changes. *Hearing research*, *115*(1-2), 101–112.

Heredia, A., Bui, C. C., Suter, U., Young, P., & Schäffer, T. E. (2007). Afm combines functional and morphological analysis of peripheral myelinated and demyelinated nerve fibers. *Neuroimage*, *37*(4), 1218–1226.

Holland, M., Budday, S., Goriely, A., & Kuhl, E. (2018). Symmetry breaking in wrinkling patterns: Gyri are universally thicker than sulci. *Physical review letters*, *121*(22), 228002.

Horn, B. K., & Schunck, B. G. (1981). Determining optical flow. *Artificial intelligence*, *17*(1-3), 185–203.

Hribar, M., Šuput, D., Carvalho, A. A., Battelino, S., & Vovk, A. (2014). Structural alterations of brain grey and white matter in early deaf adults. *Hearing research*, *318*, 1–10.

Jiang, J., Zhu, W., Shi, F., Liu, Y., Li, J., Qin, W., Li, K., Yu, C., & Jiang, T. (2009). Thick visual cortex in the early blind. *Journal of Neuroscience*, *29*(7), 2205–2211.

Jin, X., Zhu, F., Mao, H., Shen, M., & Yang, K. H. (2013). A comprehensive experimental study on material properties of human brain tissue. *Journal of biomechanics*, *46*(16), 2795–2801.

Jones, S. E., Buchbinder, B. R., & Aharon, I. (2000). Three-dimensional mapping of cortical thickness using laplace's equation. *Human brain mapping*, *11*(1), 12–32.

Klinke, R., Kral, A., Heid, S., Tillein, J., & Hartmann, R. (1999). Recruitment of the auditory cortex in congenitally deaf cats by long-term cochlear electrostimulation. *science*, *285*(5434), 1729–1733.

Koch, E. W., & Rosolowsky, E. W. (2015). Filament identification through mathematical morphology., *452*, 3435–3450. https://doi.org/10.1093/mnras/stv1521

Kohrman, D. C., Borges, B. C., Cassinotti, L. R., Ji, L., & Corfas, G. (2021). Axon–glia interactions in the ascending auditory system. *Developmental Neurobiology*.

Korver, A. M., Smith, R. J., Van Camp, G., Schleiss, M. R., Bitner-Glindzicz, M. A., Lustig, L. R., Usami, S.-i., & Boudewyns, A. N. (2017). Congenital hearing loss. *Nature reviews Disease primers*, *3*(1), 1–17.

Kral, A, Hartmann, R, Tillein, J, Heid, S, & Klinke, R. (2000). Congenital auditory deprivation reduces synaptic activity within the auditory cortex in a layer-specific manner. *Cerebral cortex*, *10*(7), 714–726.

Kral, A, Hartmann, R, Tillein, J, Heid, S, & Klinke, R. (2002). Hearing after congenital deafness: Central auditory plasticity and sensory deprivation. *Cerebral Cortex*, *12*(8), 797–807.

Kral, A., Tillein, J., Heid, S., Klinke, R., & Hartmann, R. (2006). Cochlear implants: Cortical plasticity in congenital deprivation. *Progress in brain research*, *157*, 283–402.

Kriegstein, A., Noctor, S., & Martínez-Cerdeño, V. (2006). Patterns of neural stem and progenitor cell division may underlie evolutionary cortical expansion. *Nature Reviews Neuroscience*, *7*(11), 883–890.

Kruse, S. A., Rose, G. H., Glaser, K. J., Manduca, A., Felmlee, J. P., Jack Jr, C. R., & Ehman, R. L. (2008). Magnetic resonance elastography of the brain. *Neuroimage*, *39*(1), 231–237.

Leake, P. A., Hradek, G. T., & Snyder, R. L. (1999). Chronic electrical stimulation by a cochlear implant promotes survival of spiral ganglion neurons after neonatal deafness. *Journal of Comparative Neurology*, *412*(4), 543–562.

Leprince, Y., Poupon, F., Delzescaux, T., Hasboun, D., Poupon, C., & Riviere, D. Combined laplacian-equivolumic model for studying cortical lamination with ultra high field mri (7 t). In: *2015 ieee 12th international symposium on biomedical imaging (isbi)*. IEEE. 2015, 580–583.

Liu, J., Liu, W., Yang, L., Wu, Q., Zhang, H., Fang, A., Li, L., Xu, X., Sun, L., Zhang, J., et al. (2017). The primate-specific gene tmem14b marks outer radial glia cells and promotes cortical expansion and folding. *Cell stem cell*, *21*(5), 635–649.

Long, P., Wan, G., Roberts, M. T., & Corfas, G. (2018). Myelin development, plasticity, and pathology in the auditory system. *Developmental neurobiology*, *78*(2), 80–92.

Lorensen, W. E., & Cline, H. E. (1987). Marching cubes: A high resolution 3d surface construction algorithm. *ACM siggraph computer graphics*, *21*(4), 163–169.

Lyu, I. (2017). *Cortical surface registration and shape analysis* (Doctoral dissertation). The University of North Carolina at Chapel Hill.

Lyu, I., Kim, S. H., Girault, J. B., Gilmore, J. H., & Styner, M. A. (2018). A cortical shape-adaptive approach to local gyrification index. *Medical image analysis*, *48*, 244–258.

Makinodan, M., Rosen, K. M., Ito, S., & Corfas, G. (2012). A critical period for social experience–dependent oligodendrocyte maturation and myelination. *science*, *337*(6100), 1357–1360.

Mancini, M., Casamitjana, A., Peter, L., Robinson, E., Crampsie, S., Thomas, D. L., Holton, J. L., Jaunmuktane, Z., & Iglesias, J. E. (2020). A multimodal computational pipeline for 3d histology of the human brain. *Scientific reports*, *10*(1), 1–21.

Mann, H. B., & Whitney, D. R. (1947). On a test of whether one of two random variables is stochastically larger than the other. *The annals of mathematical statistics*, 50–60.

Manno, F. A., Rodríguez-Cruces, R., Kumar, R., Ratnanather, J. T., & Lau, C. (2021). Hearing loss impacts gray and white matter across the lifespan: Systematic review, meta-analysis and meta-regression. *NeuroImage*, 117826.

McCracken, P. J., Manduca, A., Felmlee, J., & Ehman, R. L. (2005). Mechanical transient-based magnetic resonance elastography. *Magnetic Resonance in Medicine: An Official Journal of the International Society for Magnetic Resonance in Medicine*, *53*(3), 628–639.

McMullen, N., Goldberger, B, Suter, C., & Glaser, E. (1988). Neonatal deafening alters nonpyramidal dendrite orientation in auditory cortex: A computer microscope study in the rabbit. *Journal of Comparative Neurology*, *267*(1), 92–106.

Miller, D. J., Lackey, E. P., Hackett, T. A., & Kaas, J. H. (2013). Development of myelination and cholinergic innervation in the central auditory system of a prosimian primate (otolemur garnetti). *Journal of Comparative Neurology*, *521*(16), 3804–3816.

Nichols, T. E., Das, S., Eickhoff, S. B., Evans, A. C., Glatard, T., Hanke, M., Kriegeskorte, N., Milham, M. P., Poldrack, R. A., Poline, J.-B., et al. (2017). Best practices in data analysis and sharing in neuroimaging using mri. *Nature neuroscience*, *20*(3), 299–303.

Ouda, L., Burianová, J., Balogová, Z., Lu, H. P., & Syka, J. (2016). Structural changes in the adult rat auditory system induced by brief postnatal noise exposure. *Brain Structure and Function*, *221*(1), 617–629.

Prange, M. T., & Margulies, S. S. (2002). Regional, directional, and age-dependent properties of the brain undergoing large deformation. *Journal of biomechanical engineering*, *124*(2), 244–252.

Purves, D., Augustine, G. J., Fitzpatrick, D., Hall, W. C., LaMantia, A.-S., McNamara, J. O., & White, L. E. (2008). Neuroscience. 4th. *Sunderland, Mass.: Sinauer. xvii*, *857*, 944.

Ramer, U. (1972). An iterative procedure for the polygonal approximation of plane curves. *Computer graphics and image processing*, *1*(3), 244–256.

Ratnanather, J. T. (2020). Structural neuroimaging of the altered brain stemming from pediatric and adolescent hearing loss—scientific and clinical challenges. *Wiley Interdisciplinary Reviews: Systems Biology and Medicine*, *12*(2), e1469.

Ratnanather, J. T., Arguillère, S., Kutten, K. S., Hubka, P., Kral, A., & Younes, L. 3d normal coordinate systems for cortical areas. In: *Mathematics of shapes and applications*. World Scientific, 2020, pp. 167–179.

Ratnanather, T, Barta, P., Honeycutt, N., Lee, N, Morris, H., Dziorny, A., Hurdal, M., Pearlson, G., & Miller, M. (2003). Dynamic programming generation of boundaries of local coordinatized submanifolds in the neocortex: Application to the planum temporale. *NeuroImage*, *20*(1), 359–377.

Reillo, I., de Juan Romero, C., García-Cabezas, M. Á., & Borrell, V. (2011). A role for intermediate radial glia in the tangential expansion of the mammalian cerebral cortex. *Cerebral cortex*, *21*(7), 1674–1694.

Richman, D. P., Stewart, R. M., Hutchinson, J. W., & Caviness, V. S. (1975). Mechanical model of brain convolutional development. *Science*, *189*(4196), 18–21.

Ryugo, D. K., & Menotti-Raymond, M. (2012). Feline deafness. *Veterinary Clinics: Small Animal Practice*, *42*(6), 1179–1207.

Ryugo, D. K., Pongstaporn, T, Huchton, D., & Niparko, J. K. (1997). Ultrastructural analysis of primary endings in deaf white cats: Morphologic alterations in endbulbs of held. *Journal of Comparative Neurology*, *385*(2), 230–244.

Schiesser, W. E. (2012). *The numerical method of lines: Integration of partial differential equations*. Elsevier.

Schregel, K., née Tysiak, E. W., Garteiser, P., Gemeinhardt, I., Prozorovski, T., Aktas, O., Merz, H., Petersen, D., Wuerfel, J., & Sinkus, R. (2012). Demyelination reduces brain parenchymal stiffness quantified in vivo by magnetic resonance elastography. *Proceedings of the National Academy of Sciences*, *109*(17), 6650–6655.

Sethian, J. A. (1999). Fast marching methods. *SIAM review*, *41*(2), 199–235.

Sethian, J. A., & Popovici, A. M. (1999). 3-d traveltime computation using the fast marching method. *Geophysics*, *64*(2), 516–523.

Smith, K. M., Mecoli, M. D., Altaye, M., Komlos, M., Maitra, R., Eaton, K. P., Egelhoff, J. C., & Holland, S. K. (2011). Morphometric differences in the heschl's gyrus of hearing impaired and normal hearing infants. *Cerebral Cortex*, *21*(5), 991–998.

Student. (1908). The probable error of a mean. *Biometrika*, 1–25.

Sullivan, J. M. Curvatures of smooth and discrete surfaces. In: *Discrete differential geometry*. Springer, 2008, pp. 175–188.

Sunnerberg, J. P., Moore, P., Spedden, E., Kaplan, D. L., & Staii, C. (2019). Variations of elastic modulus and cell volume with temperature for cortical neurons. *Langmuir*, *35*(33), 10965–10976.

Tallinen, T., Chung, J. Y., Biggins, J. S., & Mahadevan, L. (2014). Gyrification from constrained cortical expansion. *Proceedings of the National Academy of Sciences*, *111*(35), 12667–12672.

Tallinen, T., Chung, J. Y., Rousseau, F., Girard, N., Lefèvre, J., & Mahadevan, L. (2016). On the growth and form of cortical convolutions. *Nature Physics*, *12*(6), 588–593.

Tarabichi, O., Kozin, E. D., Kanumuri, V. V., Barber, S., Ghosh, S., Sitek, K. R., Reinshagen, K., Herrmann, B., Remenschneider, A. K., & Lee, D. J. (2018). Diffusion tensor imaging of central auditory pathways in patients with sensorineural hearing loss: A systematic review. *Otolaryngology–Head and Neck Surgery*, *158*(3), 432–442.

Thirion, J.-P. (1998). Image matching as a diffusion process: An analogy with maxwell's demons. *Medical image analysis*, *2*(3), 243–260.

Toro, R., & Burnod, Y. (2005). A morphogenetic model for the development of cortical convolutions. *Cerebral cortex*, *15*(12), 1900–1913.

Van Essen, D. C. (1997). A tension-based theory of morphogenesis and compact wiring in the central nervous system. *Nature*, *385*(6614), 313–318.

Velardi, F, Fraternali, F, & Angelillo, M. (2006). Anisotropic constitutive equations and experimental tensile behavior of brain tissue. *Biomechanics and modeling in mechanobiology*, *5*(1), 53–61.

Waehnert, M., Dinse, J., Weiss, M., Streicher, M. N., Waehnert, P., Geyer, S., Turner, R., & Bazin, P.-L. (2014). Anatomically motivated modeling of cortical laminae. *Neuroimage*, *93*, 210–220.

Welch, B. L. (1947). The generalization of student's' problem when several different population variances are involved. *Biometrika*, *34*(1/2), 28–35.

Welker, W. (1990). Why does cerebral cortex fissure and fold?, 3–136.

Xu, G., Knutsen, A. K., Dikranian, K., Kroenke, C. D., Bayly, P. V., & Taber, L. A. (2010). Axons pull on the brain, but tension does not drive cortical folding. *Journal of biomechanical engineering*, *132*(7).

Yang, J., Mandriota, N., Harrellson, S. G., Jones-Molina, J. A., Yuste, R., Lefort, R., & Sahin, O. (2020). Extreme stiffness of neuronal synapses and implications for synaptic adhesion and plasticity. *bioRxiv*.

Yousefsani, S. A., Farahmand, F., & Shamloo, A. (2018). A three-dimensional micromechanical model of brain white matter with histology-informed probabilistic distribution of axonal fibers. *Journal of the mechanical behavior of biomedical materials*, *88*, 288–295.

Biography

Qianwei Li was born in Shanxi, China in 1997. She graduated from the University of Science and Technology of China with a B.S. in Applied Physics in 2019. She focused on fast 3D reconstruction, registration, and neuron tracing for ultrahigh-speed brain mapping during her undergraduate research. In the summer of 2019, she joined the M.S.E. program in Biomedical Engineering at Johns Hopkins University. During the program, she conducted research on mathematical analysis of neuroimaging under the supervision of Dr. Tilak Ratnanather. Qianwei Li is broadly interested in brain mapping, image processing, computational modeling and machine learning.